Effects of Local Processing Parameters on Microstructure, Texture, and Mechanical Properties of Electron Beam Powder Bed Fusion Manufactured Ti-6Al-4V

Edwin J. Schwalbach[1,*,†], Jake T. Benzing[2,*,‡], Vikas Sinha[1,3,§], Todd M. Butler[1], Adam L. Pilchak[1,§], Kevin J. Chaput[1,**], Norman D. Schehl[1,4], Reji John[1], Nikolas Hrabe[2]

1. Air Force Research Laboratory, Materials and Manufacturing Directorate, Wright-Patterson Air Force Base, OH 45433, USA
2. National Institute of Standards and Technology, Applied Chemicals and Materials Division, Boulder, CO 80305, USA
3. UES, Inc., 4401 Dayton-Xenia Road, Dayton, OH 45432, USA
4. University of Dayton Research Institute, 300 College Park, Dayton, OH 45469, USA

Abstract

Electron beam powder bed fusion scan strategies for parts or part groupings of various sizes and scan line lengths have been found to inadvertently lead to significant variations in crystallographic texture and mechanical properties for Ti-6Al-4V. This occurs over a range of scan line length that is well below the maximum scan line length recommended by the electron-beam powder bed fusion machine manufacturer. The microstructural attributes such as α lath thickness, prior β grain size, and β phase fraction were similar for materials fabricated under short and long scan line length conditions, but the crystallographic textures varied considerably. Electron backscatter diffraction measurements indicate the basal pole $[0001]_\alpha$ was strongly aligned with the build direction for long scan line length conditions, whereas $\langle 11\bar{2}0\rangle_\alpha$ were aligned with the build direction for short scan line length conditions. Subsequent prior β reconstructions indicate a preference for alignment of $\langle 110\rangle_\beta$ and $\langle 100\rangle_\beta$ with build direction for long and short scan line length conditions, respectively. Both yield and ultimate tensile strengths along the build direction were approximately 8% higher for long scan line lengths, consistent with the observed differences in texture. The impact of a sub-solvus hot isostatic pressing was also investigated, however, this did not significantly change the textures of as-built materials or the relative strengths for the two processing conditions.

Keywords: Additive Manufacturing, titanium alloy, electron backscatter diffraction (EBSD), preferred orientation, scan line length

1 Introduction

Electron beam powder bed fusion (EBPBF, sometimes referred to as electron beam melting, EBM) is a common method to additively manufacture titanium components [1]. The material properties and performance of parts produced using the common titanium alloy Ti-6Al-4V are intimately

* These authors contributed equally
† edwin.schwalbach@us.af.mil
‡ jake.benzing@nist.gov
§ Present address: Materials Resources LLC, 123 Fairground Rd, Xenia, OH 45385, USA
** Present address: Northrop Grumman Corp. Melbourne, FL 32901, USA

related to a number of details of the alloy's microstructure [2]. While a number of studies have investigated the microstructure and properties resulting from EBPBF of Ti-6Al-4V [3]–[11], the combination of the complexity of both the material itself and the EBPBF process have led to a range of reported behaviors. In particular, inter-relationships between processing parameters [3], [6], [11] and parameter dependencies on component geometry [5], [10] have all been shown to influence structure and properties. The present work aims to describe the relationship between part geometry and processing parameters, and their influences on crystallographic texture.

A series of phase transformations occur on cooling Ti-6Al-4V from the molten state to room temperature which control final microstructure and ultimately properties [2]. The first solid phase to form during solidification of Ti-6Al-4V is the body centered cubic (*bcc)* β phase. A significant fraction of β phase transforms either to the hexagonal close packed (*hcp*) α*'*-martensite upon fast cooling (e.g. $\gtrsim 1000$C/s) to a temperature below the martensite-start temperature (M_s), or to *hcp* α phase upon slow cooling below the β-transus (T_β) temperature. A small fraction of β is retained in the equilibrium structure at room temperature. In many instances, α*'*-martensite (if formed initially due to fast cooling rates) subsequently transforms to α due to heating caused by printing of subsequent layers [8]. The final microstructure formed by EBPBF primarily consists of α and β because the powder bed is kept at a temperature higher than $M_s \approx 575$ °C [12], [13] through a bed preheating process [9].

The transformed α and parent β phases follow the Burgers orientation relationship [14]–[16], where $(0001)_\alpha \parallel \{110\}_\beta$, and $\langle 11\bar{2}0\rangle_\alpha \parallel \langle 111\rangle_\beta$. As a result, the crystallographic texture of prior β phase formed during the initial solidification process plus any variant selection effect during the $\beta \rightarrow \alpha$ phase transformation dictate the room temperature α phase texture,. The prior β grain morphology and texture are controlled by the details of solidification [17]–[20] and therefore, EBPBF processing conditions. The β phase in room temperature microstructures is typically sparse and distributed, which makes the direct characterization of prior β phase textures with techniques such as electron backscatter diffraction (EBSD) challenging. However, the grain morphology and texture of prior β can be assessed via reconstructions of the EBSD data collected on the room temperature α phase [1], [4], [5].

The elastic and plastic properties of α phase are crystallographically anisotropic [2], [21], [22]. As a result, the mechanical properties of additively manufactured Ti-6Al-4V parts are expected to vary with the texture of α phase, which constitutes the majority of the room temperature microstructure. Such dependence has previously been reported for unidirectionally rolled Ti-6Al-4V which exhibits significant crystallographic texture as a result of deformation processing [23]. Specifically, higher strengths and lower fatigue lives were reported when $[0001]_\alpha$ is preferentially aligned with the loading axis, compared with a test condition where this direction is preferentially perpendicular to the loading axis.

The majority of previous studies for EBPBF Ti-6Al-4V have reported a texture where $\langle 100\rangle_\beta$ is aligned with the build direction [4], [5], [24], though a few studies have reported other textures [7], [25]. In an investigation on EBPBF Ti-6Al-4V, Draper, et al. [7] reported that $[0001]_\alpha$ was preferentially aligned with the build direction for one build and was randomly distributed for a second build, based on X-ray diffraction measurements. While they did not report prior β

orientation, assuming a Burgers orientation relationship [14]–[16] between prior β and transformed α, $\langle 110 \rangle_\beta$ of prior β is expected to be preferentially aligned with the build direction for the first build in that study [7]. In another study on EBPBF Ti-6Al-4V, Hrabe, et al. [25] conducted EBSD characterizations directly for the β phase in room-temperature microstructures at a fine step size of 30 nm and reported that a mixture of $\langle 100 \rangle_\beta$, $\langle 110 \rangle_\beta$, and $\langle 111 \rangle_\beta$ was aligned with the build direction. Further, for the as-built materials, $\langle 100 \rangle_\beta$ was reported to be preferentially aligned with build direction for vertical specimen geometry and $\langle 110 \rangle_\beta$ was reported to be preferentially aligned with build direction for horizontal specimen geometry [25]. The results in Refs. [7], [25] differ from those of [4], [5], [24], which reported a preferential alignment of $\langle 100 \rangle_\beta$ with the build direction. It is also worth noting that β textures reported in reference [25] were from direct EBSD measurements on β phase at room temperature, whereas those reported in references [4], [5], [24] were from prior β reconstructions performed on EBSD data collected on room temperature α phase.

We also note that studies in other materials that solidify with the BCC structure have reported different preferred orientations as a function of processing conditions. In particular, a study on EBPBF of Mo indicated a dependence of the preferred orientation with respect to the build direction as a function of processing parameter changes in EBPBF [26]. Specifically, a variation from $\langle 100 \rangle$ to $\langle 111 \rangle$ along the build direction was reported as a function of increasing energy per unit area employed during the EBPBF process.

The laser powder bed fusion (LPBF) methods are another important group of AM technologies for fabricating titanium alloy products, and it is relevant to compare the texture evolution produced by LPBF and EBPBF. LPBF processing uses optical mirrors to steer the energy source, which leads to slower overall scan speeds, when compared to the electromagnetic coils used in EBPBF. Perhaps the largest difference in processing is the use of a high background temperature in EBPBF, which reduces the martensite fraction in Ti-6Al-4V, especially when compared to LPBF [27]. The prior studies on LPBF of titanium alloys have reported a texture where $\langle 100 \rangle_\beta$ is either preferentially aligned with the build direction [28], [29] or slightly misoriented from the build direction [30], [31]. In particular, $\langle 100 \rangle_\beta$ was reported to be aligned with the build direction for a β-titanium alloy, Ti-Cr [28], as well as for an ($\alpha + \beta$) titanium alloy, TC21 (i.e., Ti–6Al–2Zr–2Sn–3Mo–1.5Cr–2Nb) [29]. In Ti-6Al-4V additively manufactured with LPBF, the $\langle 100 \rangle_\beta$ was reported to be aligned with the prior-β grain growth direction, which was inclined approximately 20° with respect to the build direction [30], [31]. Others have also reported the ability to manipulate crystallographic texture from $\langle 100 \rangle$ to a mixed $\langle 110 \rangle + \langle 100 \rangle$ along the build direction in 316L stainless steel parts produced with LPBF by manipulating the hatch scan strategy [32].

The current study was conducted to systematically assess variations in microstructure, texture, and mechanical properties of Ti-6Al-4V additively manufactured with EBPBF due to variations in the part geometry, specifically the scan line length. We expect these relationships will be useful to understand the effect of processing, to inform future process design, to minimize inadvertent changes in part reliability, and to maximize mechanical performance.

2 Methods

2.1 Sample fabrication with electron beam powder bed fusion

Two sets of specimens fabricated using A-series Arcam[††] EBPBF equipment will be referred to as set 1 and set 2 throughout this article. Table 1 describes several key processing attributes, and the full list of parameters are given in Supplementary Table 1. Figure 1 shows isometric and top-down views of the build geometries.

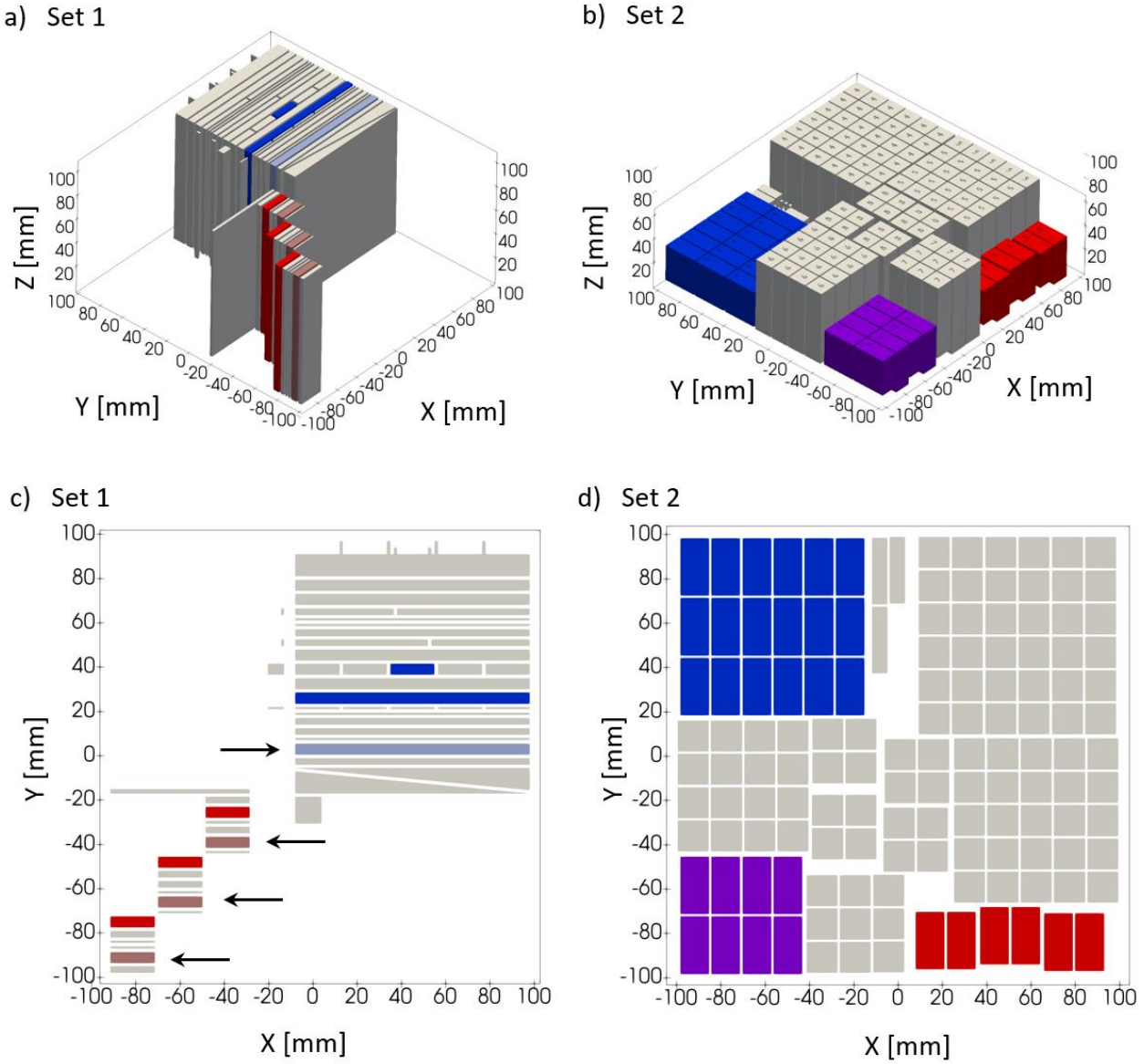

Figure 1: Oblique and top-down views of the builds for specimen set 1 (a,c) and set 2 (b,d). Test specimens were excised from colored regions. Blue indicates objects with the largest scan line length, and red the shortest scan line

[††] Certain commercial software, equipment, instruments or materials are identified in this paper in order to adequately specify the experimental procedure. Such identification is not intended to imply recommendation or endorsement by the National Institute of Standards and Technology or the United States Air Force, nor is it intended to imply that the equipment or materials identified are necessarily the best available for the purpose.

length within each set, and purple is used for an intermediate scan line length in set 2 only. For specimen set 1, shading and annotation arrows denote specimens that were subjected to a HIP treatment.

EBPBF generally proceeds as follows; powder feed stock and a steel build-plate are loaded into the machine and a vacuum is established. The electron beam is defocused and repeatedly rastered quickly over the entire build plate to preheat it. When the plate temperature reaches approximately 730 °C as measured by a thermocouple on the bottom of the plate, the actual build process begins. At the beginning of each layer, the build plate moves downward by an amount equal to the layer thickness, and then powder is spread from hoppers on either side of the build table with a rake mechanism. The electron beam is again defocused and quickly rastered over the powder layer bed several times to heat and sinter the layer of powder using a predefined procedure. Once this layerwise preheating procedure is completed, the machine proceeds using a focused e-beam to scan first the contours (exterior surfaces) of all bodies, before finally processing the bulk or interior region of the 2D slice. Additional preheating operations may be executed either between the processing of bodies, or after the completion of all other operations but before beginning the next layer. This process repeats successively until all layers have been completed, at which point the build is allowed to slowly cool in an inert environment.

The processing of the interior or bulk region of individual components is complex. For the systems used in this study, scan vectors rotate by 90° between successive layers, being generally either parallel or antiparallel to the machine's *X* and *Y* directions using the standard coordinate system which is shown in Figure 1 and defined in detail in Ref. [33]. Solid bodies to be printed are assigned to *melt groups* (also known as melt models), operator defined collections of items to which a specific set of processing parameters will be applied. While these user controllable parameters affect the processing conditions, in particular the power P and scan velocity v, the system uses a proprietary algorithm to select the actual parameter values based on the *scan line length* as discussed by several other reports [3], [6], [10], [11]. This length is measured individually for each scan vector along the direction of beam travel across all objects within the melt group, excluding any gaps between parts or the region affected by the contouring process.

Because the processing conditions are determined not only by global parameters but also scan line length, the particular spatial arrangement of bodies as well as their operator-determined assignments into melt groups can affect local processing history, and therefore potentially the microstructure and properties of the material produced. Color in Figure 1 denotes solid bodies that are collected into melt groups to control scan line length. Red denotes the shortest scan line length in each build, blue the longest, and purple is used for an intermediate scan line length in set 2. Also, in set 2 the 6 red items that constitute the short line length group are collected into 3 sets of pairs, with all three sets having the same line length.

To assess the impact of this processing nuance, in specimen set 1 all bodies were included in a single melt group, and the scan line length was manipulated to either a long or short value by simply selecting the size and arrangement of bodies. The scan line lengths for a given body are similar in both the *X* and *Y* directions, though not identical. For specimen set 2, the scan line length was manipulated by replicating and arranging varying numbers of copies of the same solid body into three different melt groups. While other bodies were present in the build, these were not included in the melt groups that produced the tensile and microstructure specimens described here, and thus did not contribute to their scan line lengths.

Finally, note that the particular details described above are specific to the proprietary control algorithm used in the particular equipment in question. All details of this algorithm are not fully known to the authors, and furthermore are subject to change as new models and control software updates are issued. For this reason, an empirical technique described in Section 2.4 is used to estimate the actual processing parameters for each body.

Parameters	**Set 1**	**Set 2**
Model	Arcam A2	Arcam A1
Machine Name, S/N	R1057	R1074
Control software version	3.2.142.14622	3.2.132.14429
Processing theme version	3.2.121	3.2.121_EXT3
Ti-6Al-4V Powder Composition [1]	Grade 5	Grade 23
Layer Thickness [μm]	50	50
Hatch spacing [μm]	100	100
Speed Function	98	76

Table 1: Selected processing details for specimen sets 1 and 2. Full parameter sets are listed in Supplementary Table 1. Chemistry specification and measured powder compositions are listed in Table 3.

Gas atomized powders with chemical compositions consistent with the Ti-6Al-4V grades listed in Table 1 were employed. The starting powder compositions were within the specifications of ASTM B348 for their respective grades [34]. Post-build chemistry was also measured as discussed in Section 3.1. In general, powder morphology was spherical with few satellites, and the particle size range was approximately 40 μm to 100 μm for both specimen sets.

A subset of items from specimen set 1 were hot-isostatic pressed (HIP) before any machining or specimen cutup was performed. Individual plates were wrapped in Ta foil and loaded into a graphite fixture that held them upright and spaced apart in the HIP vessel. The vessel was closed and brought to vacuum below 7 Pa followed by three purges using ultra-high purity argon. A sub-solvus HIP was performed with a soak at 900 °C and 100 MPa for 240 minutes consistent with AMS 4992C [35]. An initial high heating rate was used to reduce heat-up time, but was decreased as temperature approached the set point to minimize temperature overshoot, and in particular to ensure that the β-transus temperature was not exceeded. The material was cooled in the vessel under inert atmosphere.

2.2 Microstructural Characterization

All microstructural characterization data was generated for material that was adjacent to the tensile specimen gage region, which corresponded to a height from build plate (Z) of approximately 53 mm for specimen set 1, and Z=20 mm for specimen set 2. For specimen set 1, material was initially removed from the tensile blanks via wire electrical discharge machining (EDM) as described in Section 2.3. Metallographic specimens were further excised using a low-speed diamond saw, and then hot mounted in phenolic resin before polishing with standard metallographic techniques. Final polishing was conducted using 0.05 μm non-crystallizing colloidal silica in a vibratory polisher for both sets 1 and 2.

2.2.1 Porosity Characterization

Samples of each material condition were analyzed for internal porosity with an X-ray computed tomography (CT) machine (Zeiss XRadia) with the following parameters: 160 kV, 10 W, 1 μm voxel size. The ImageJ (Fiji) 3D Objects Counter plugin was used to quantify the pore sizes and morphologies, and the Volume Viewer plugin was used to create pore projection images [36]. Measured pore volume was converted to an estimated equivalent spherical diameter for all pores, and pore density was plotted as a function of pore diameter. Also, all pores were classified using aspect ratio (major axis divided by minor axis of the best fitting ellipsoid) as either a gas pore (aspect ratio less than 2) or a lack of fusion (LOF) pore (aspect ratio greater than or equal to 2). Finally, the volumetric percentage of porosity of each specimen was calculated using the total volume of the CT scan and the total volume of the pores. One specimen from each scan line length was analyzed via CT. For set 1, material directly adjacent to tensile specimen gage sections were analyzed, and for set 2 the gage section was analyzed directly.

2.2.2 α-Lath Thickness, Prior-β Width and Texture Characterization

To determine the average Widmanstätten α-phase lath thickness for each specimen, a series of six, electron-backscattered diffraction (EBSD) maps each covering a square area with edge length 42 μm to 50 μm were captured using TSL OIM™ Data Collection software on a PHILIPS/FEI XL-30 SEM (FEI Company, Hillsboro, OR). These maps were taken at least 1 mm in from the free surface to ensure only microstructure from bulk scanning regions were captured. The EBSD maps, comprising both the α and β phases, were collected with an accelerating voltage of 10 kV and a step size of 100 nm. All scans were conducted at an SEM stage tilt of 70° and at a working distance of 25 mm. All maps and pole figures were generated and investigated using the EDAX/TSL OIM™ Analysis 7 software package (EDAX Inc., Mahwah, NJ). Binary images were created that identify boundaries from the α phase maps and fill in regions identified as β phase. These binary images were then digitally processed using Adobe Photoshop™ 12.0.4 equipped with the Fovea Pro™ Beta 5 plug-in package. Each image was first calibrated for length using a SEM image captured from a Geller magnification calibration standard and then inverted to reverse the contrast (α black / β white).

In order to calculate the average α-lath thicknesses from the binary images, an intercept technique using the IP*Global measure-intercepts plug-in was employed. This method overlays an inclined grid of parallel lines onto each image and automatically segments the lines across α/β-phase boundaries and over distinct β-phase regions. The remaining line segments, representative of exclusively α-phase regions, are then measured and binned. This process is repeated for grid inclination angles of 5° to 175° in 10° increments. The intercept lengths were then inverted, and the mean inverse intercept was used to determine the true α-lath thickness t_α for each image according to

$$t_\alpha = \frac{1}{1.5\left(\frac{1}{\lambda}\right)_{\text{mean}}} \quad (1)$$

where λ is the line intercept length. The basis of this relationship stems from the notion that the true thickness of an infinite set of plates can be estimated with line segments generated by intersections with parallel lines at a set inclination angle [37]–[40]. This method accounts for the thickness of the β-phase and generates statistically relevant datasets (order of 30,000 intercepts for a single image) in an efficient and automated manner.

To determine prior grain width, several *YZ* slices were etched using Keller's Reagent (95 ml water, 2.5 ml HNO_3, 1.5 ml HCL, 1.0 ml HF). A series of five horizontal lines with known lengths were then drawn perpendicular to the columnar grains at various *Z* heights and the respective columnar β-grain boundaries were manually identified on each line. The total number of intercepts for each line was then used to determine the average intercept length, corresponding to the mean width of a columnar β-grain.

Finally, mosaic, large-area EBSD scans were conducted on each material condition and encompassed at least 10 mm^2 in area each. The measurements were performed to assess texture with a FE-SEM: 20 kV, 7.8 nA current, and a 25 mm working distance. A step size between 1.2 and 2.0 µm was used to capture global texture in each 450 µm × 450 µm tile. Automated stage movements were used to facilitate large area EBSD scans, which were stitched into continuous maps for further analysis [41], [42]. Texture calculations were performed by a harmonic series expansion of all measurement points, including assumption of a triclinic sample symmetry to minimize loss during subsequent reconstruction processes, a 16 series rank, and a 5 degree Gaussian half-width resolution [43].

2.2.3 Prior β reconstructions

In order to effectively understand the manifestation of the α-phase texture and its correlation to the processing conditions, it was necessary to examine the β-phase texture. Using a previously developed method outlined in Ref. [44] and which relies on Burgers Orientation Relationship (BOR) between the α-phase and parent β-phase, large area α-phase EBSD maps described in the previous section were inverted to generate corresponding prior β-phase map using the commercial software TiBOR (Materials Resources LLC, Dayton, OH) [44]–[48].

The fields of view employed for reconstructions of set 1 included both interior or 'bulk' regions as well as contour, whereas those for set 2 only included bulk regions more than 500 µm from the free surface. To appropriately capture the relative area of bulk and contour affected regions present in the tensile gage section for set 1, the region analyzed via EBSD was cropped to include half the thickness of the specimen. Specifically, a region of interest was selected that extended from the free surface inward toward the centerline by a distance of 2.5 mm. An additional smaller region of interest that includes only bulk material is also considered, as will be discussed in Section 3.2.3.

2.3 Tension tests

Two mechanical test specimen geometries were used to develop monotonic tensile properties, as shown in Figure 2. Specimens from set 1 were extracted from nominally 5 mm thick plates using EDM. All plates measured 106 mm in the build direction and either 106 mm or 20 mm along the *X* direction, with a total of 10 specimens coming from the larger plates, and 6 from the smaller plates. Surfaces that were not machined retained the as-built finish. The surfaces of the gage-section that were machined were finished with a low-stress grind, parallel to the loading direction. The final specimen gage sections have width of 6.50 mm and a length of 16.0 mm; specimen thickness remained as-built, nominally 5 mm. For specimen set 2, ten tensile specimens were excised from the upper half of all Ti-6Al-4V parts for each material condition using EDM. Specimens are 12.7 mm total in length, with a 2.54 mm gage width and 1.27 mm thickness. In all cases for both specimen sets the tensile loading axis is parallel to the build direction *Z*.

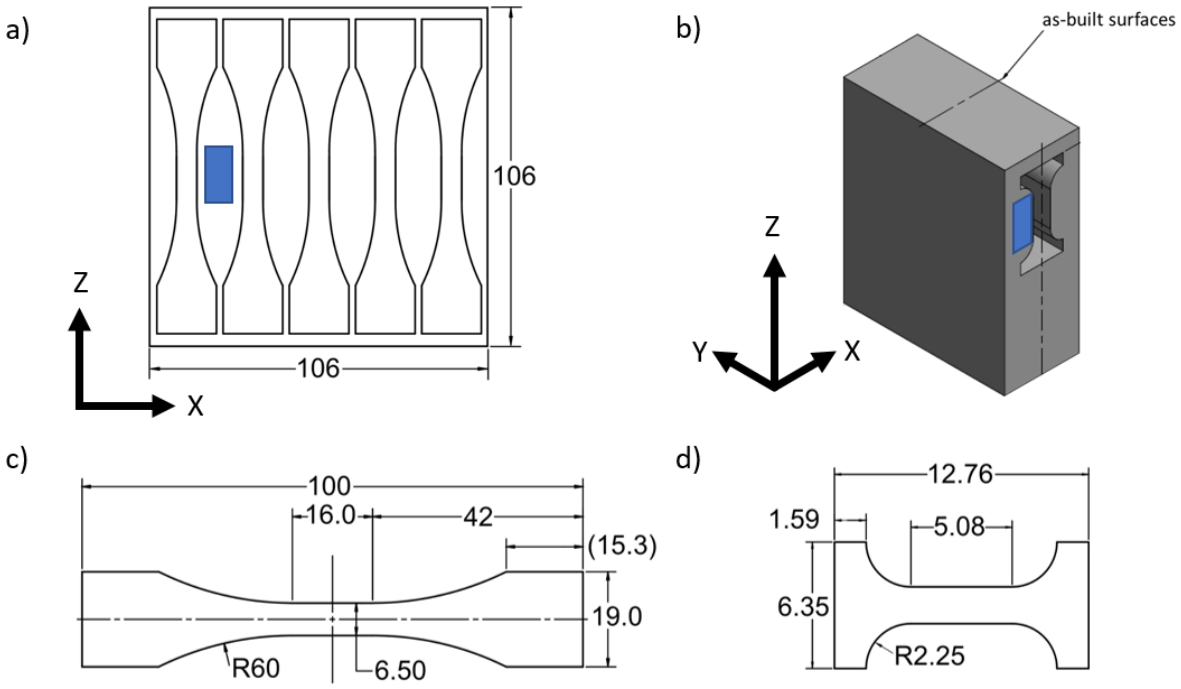

Figure 2: Mechanical test geometries (dimensions in mm) for specimen set 1 in a) and set 2 in b). Blue shaded regions indicate material used for microstructure assessments.

All uniaxial tension tests were performed with servo-hydraulic testing machines. For specimen set 1, strain was monitored using a 12.7 mm gage-length knife-edge extensometer, whereas specimens in set 2 employed an extensometer with 3 mm gage length. All tests for both sets were performed under strain control with strain rate of 10^{-3} s^{-1} in a laboratory air environment at room temperature. An analysis of variance was completed with InStat software and used to test the null hypotheses that the tensile properties were equal across material conditions; significance is $p < 0.01$.

Two measures of strain hardening behavior were computed from the raw engineering stress s and engineering strain e curves for set 1. The true strain ϵ and true stress σ were first determined according to

$$\epsilon = \ln(1 + e) \quad (2)$$

$$\sigma = s(1 + e) \quad (3)$$

for all values of e less than the strain at ultimate tensile strength, $e_{UTS} = e(\max(s))$. These data are then smoothed using 2 passes of a moving average filter with a window size of 11 data points to remove noise. The first measure of quantifying strain hardening is through estimation of the derivative $d\sigma/d\epsilon$ using a best-fit first order polynomial in a moving window across all strains less than the strain at UTS. The radius for the moving window was 100 data points. The second measure of strain hardening is through computation of a local strain hardening exponent n based on power law behavior

$$\sigma = C\,\epsilon^{n} \quad (4)$$

This quantity is computed for all $e < e_{UTS}$ using the same moving linear best-fit procedure, however the independent and dependent variables considered are $\ln \epsilon$ and $\ln \sigma$ respectively. The particular choices for the smoothing and linear fit sizes described were determined through a sensitivity analysis.

2.4 Log-file analysis

In order to characterize the processing conditions with sufficient detail and ultimately simulate the range of solidification phenomena induced, effective values for several critical processing parameters are needed. While others have reported relationships between machine settings and actual values used [3], [6], [11], there is both considerable complexity in the algorithms used as well as changes in these details over time. Therefore, in the present case these quantities are estimated empirically by analyzing the build log-files for each specimen set generated by the specific AM system. These log-files contain a record of not only all user controllable parameters, but also time-stamped lists of a range of different types of events. One such set of events includes reports of the beam current i_B, representative traces of which are shown in Figure 3 for approximately 1600 layers from specimen set 1. These layers have been separated into four sets based on the repeating rotating scan vector pattern employed. Furthermore, the absolute times t have been adjusted to put all data into unique layer-specific into time reference frame t_l , where the time origin is assigned to the beginning of the bulk scan on that layer. For clarity and to focus the analysis on the bulk scan vector, we show only the portion of the current profiles for t_l>0, thus omitting the preheat and contour scan operations. While there is some variation from layer to layer in the bulk scan portion of the profiles, Figure 3 shows that once scan orientation is accounted for the current vs. time patterns are quite regular for this geometry.

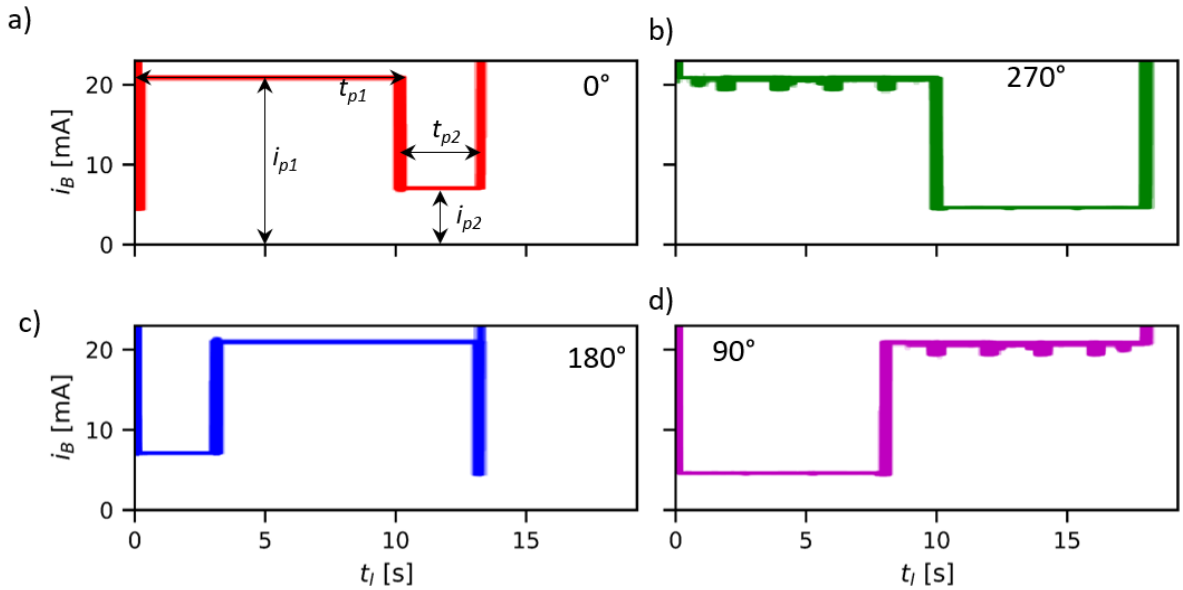

Figure 3: Beam current i_B vs. layer specific time t_l for 1600 total layers of the build for set 1 separated by the 4 unique scan orientations. The arrows in a) indicate the duration t_p and current i_p for two plateaus in layers with like scan orientation. Only scanning of bulk vectors is shown, preheating and contour operations occur at t_l<0 and are omitted for clarity.

Both specimen sets 1 and 2 contain geometries that have simple rectangular cross sections within each layer, and furthermore their edges are parallel to the X and Y directions (i.e. the scan directions). These objects are arranged spatially and within melt groups in the process control algorithm such that their scan line lengths can be easily computed. This also results in distinct plateaus in the beam current time-history as the different bodies are successively processed. These plateaus are identified in each layer in the build, and averages across several layers are taken to determine typical values of both plateau amplitude i_p and duration t_p. Because the scan strategy rotates by 90° between layers and the parameters are determined by the scan line length on each layer, averages are computed for layers with like scan rotation orientations. By mapping the different observed plateaus to geometric features in the builds, location specific average conditions are determined. The average amplitude of the plateau is taken as the effective beam current i_p, and the nominal power is then

$$P_p = i_p V_{ac} \tag{5}$$

where V_{ac} is the accelerating voltage, 60 kV for all specimens.

The average scan velocity v_p for scans of a particular orientation is

$$v_p = \frac{l_{p\perp} l_{p\parallel}}{h t_p} \tag{6}$$

where $l_{p\perp}$ and $l_{p\parallel}$ are the dimensions of the object perpendicular and parallel to the scan direction respectively, h is the hatch spacing, and t_p is the average plateau duration for the orientation. For simulation of the actual process, the values P_p and v_p must be known for each unique scan orientation. Note that $l_{p\perp}$ and $l_{p\parallel}$ are derived from the specimen geometry shown in Figure 1 and adjusted by removing a contour offset for each free surface encountered, and thus $l_{p\parallel}$ is referred to as the contour adjusted scan line length. For a given item, this quantity varies across the different scan orientations, and for brevity the notation $\overline{l_{p||}}$ is used to denote its average value across all orientations.

Note that this method gives only an estimate of the local scan velocity as t_p additionally includes both the time taken to jump over any gaps between bodies in the same melt group, as well as the process of turning the beam at the end of each scan line. The latter of these is complicated by the so-called "turning point" function which temporarily increases scan velocity after each turning event. Both of these effects will have a larger impact on accuracy as $l_{p\parallel}$ decreases. Furthermore, for arbitrary geometries processing conditions could vary in a more continuous fashion resulting in a current vs. time profile that does not generally contain distinct plateaus. A procedure to empirically determine scan line specific parameters would be significantly more complex in this scenario. Finally, note that while the majority of user controllable parameters are identical between specimen sets 1 and 2 (Table 1 in Supplementary Material), a systematic comparison of all parameters captured in the log files shows several potentially important differences. The importance of empirically establishing the scan line specific conditions is further emphasized because the algorithms that translate these settings are not generally known beyond the AM equipment manufacturer.

2.5 Process modeling

The orientation specific P and v values determined from the log-file analysis are used in a Discrete Source Model (DSM) representation of the energy input process to simulate the thermal history at a point in the center of each of the long and short geometries representative of sample set 1. The DSM is a physics-based thermal transport model that accounts for conductive transport and provides an approximation of the thermal history, the complete details of which are described in ref. [2]. The actual moving energy source is represented as a series of discretely located energy sources that are activated at appropriate times to mimic the moving beam, and analytical solutions to the thermal transport contribution of each source are summed to produce a representation of the original moving beam. This model is sensitive to layer specific P and v, as well as details of the specimen geometry and beam trajectory, but does not directly account for effects such as radiation, convective transport, evaporative cooling, or temperature dependent thermo-physical properties.

Because the critical processing parameters and scan trajectory vary on each layer, a representative X,Y location near the center of each of the long and short specimens is considered on 4 sequential layers, with the path rotating 90° between each layer. The DSM calculation is setup to identify solidification events induced by the beam on its closest pass to the location in question. The thermal field is interrogated and the melt pool width, depth and length are determined.
Table 2 shows all layer or position independent parameters employed in the DSM, and additionally the numeric parameters include a 2 mm spatial cutoff and an infinite time cutoff, the effects of which are described in more detail in Ref. [49].

Parameter	Unit	Value
Efficiency, η	-	0.5
Source size, $\sigma_x = \sigma_z$	µm	50
Property temperature, T_p	°C	1203
Density, ρ	kg m^{-3}	4252
Thermal conductivity, κ	W m^{-2} K^{-1}	22.93
Heat capacity, c_p	J kg^{-1} K^{-1}	678.6
Bed temperature, T_0	°C	700
Solidus temperature, T_s	°C	1650
Cutoff distance, R_{cut}	mm	2
Cutoff time, t_{cut}	s	∞
Source discretization, Δt	µs	20

Table 2: Layer independent parameters used in the DSM. Thermophysical parameters are based on ref. [50] and procedures in [49].

3 Results

3.1 Chemical composition of as-built materials:

Table 3 contains chemical analysis results for specimen sets 1 and 2. Specimen set 1 and 2 are consistent with Ti-6Al-4V Grade 5 and Grade 23 respectively, differing chiefly in their oxygen content in the as-built state. Additionally, comparing the powder to as-built states for specimen set 1, the EBPBF process results in an increase in oxygen content, and a slight loss of Al. Also, the chemistry in the long and short conditions within specimen set 1 are generally quite similar.

Specimen Set	Sample	Composition [weight %]							
		Al	C	N	H	O	Fe	Ti	V
1	Powder	6.45	0.02	0.02	0.002	0.15	0.19	Bal.	3.87
1	Short	5.91	0.02	0.02	0.0017	0.18	0.4	Bal.	4.11
1	Long	6.01	0.01	0.02	0.0019	0.19	0.2	Bal.	4.11
2	As-Built	5.82	0.01	0.01	0.001	0.100	0.20	Bal.	4.0
Spec. Grade 5	Max	6.75	0.08	0.05	0.015	0.20	0.40	Bal.	4.5
Spec. Grade 5	Min	5.50	-	-	-	0.13	-		3.5
Spec. Grade 23	Max	6.5	0.08	0.03	0.0125	0.13	0.25	Bal.	4.5
Spec. Grade 23	Min	5.5							3.5

Table 3: Chemistry of EBPBF Ti-6Al-4V parts (weight %). Measurements conform to ASTM B348 [34].

3.2 Microstructure

3.2.1 Porosity

Table 4 summarizes results of X-ray CT scans in the form of the specimen relative density, total porosity, and a breakdown of the porosity based on type as described in Section 2.2.1. Additionally, Figure 4a) contains visual representations of the porosity distribution for 5 unique contour adjusted scan line lengths across both sets, and Figure 4b) shows the size distributions for each of these sets.

Set	$\overline{l_{p\|\|}}$ [mm]	Pore Volume [%]		
		Total	LOF	Gas
1	81	0.095	0.006	0.089
2	69	0.143	0.000	0.143
2	46	0.093	0.000	0.093
2	23	0.114	0.001	0.114
1	16	0.033	0.004	0.028

Table 4: X-ray CT results showing total porosity across all conditions.

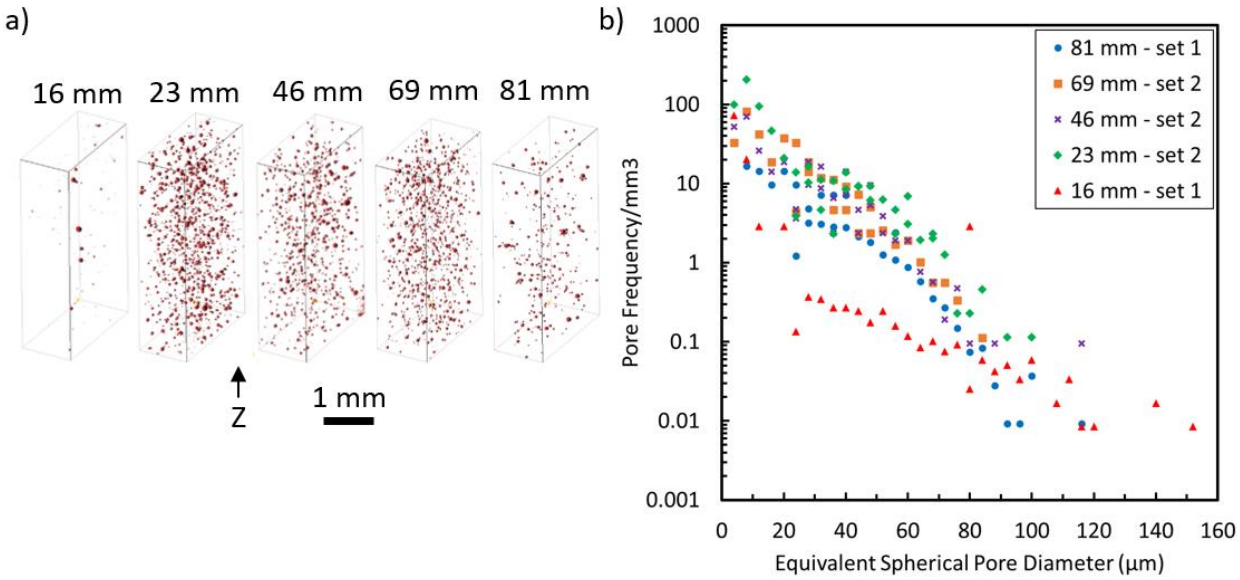

Figure 4: X-ray CT results showing a) 3D representations of porosity and b) pore size distributions for all conditions.

3.2.2 α Lath and β Grain Dimensions

Table 5 contains measures of both the α-lath thickness and β-grain width. The α-lath measurements are reported from observations on *XY* cross sections, and the β-grain width is determined from *YZ* cross sections as described in the Methods section.

Set	$\overline{l_{p\|\|}}$ [mm]	Prior β-grain width [µm]	α-lath thickness [µm]
1	81	65.6 ± 6.5	0.25
2	69	74.3 ± 16	0.35
2	46	71.4 ± 16	0.29
2	23	69.5 ± 18	0.30
1	16	61.7 ± 4.9	0.24

Table 5: α lath and prior-β grain dimensions from bulk regions. Prior-β grain width is the intercept length as viewed in the *YZ* plane, and the α-lath values are reported as viewed in *XY* planes where the true thickness is computed using Equation 1.

3.2.3 Crystallographic Texture

Figure 5 shows large-area EBSD measurements from two of the five material conditions (set 1, contour adjusted scan line lengths of 81 mm and 16 mm) in the *XY* plane, where *Z* is the build direction. The supplemental images S1 and S2 contains *YZ* views as well as additional conditions. Each inverse pole figure map was created to show the poles parallel to the same specified direction, which in this case is the build direction, *Z*. Displaying poles parallel to the same reference direction allows for continuity when deciphering the dependence of crystallographic texture on processing conditions, regardless of sample perspective (*XY* vs. *XZ*). In Figure 5a and b, the measurements of α-Ti orientations are shown above the prior-β reconstructions, seen in Figure 5c and d.

To understand the influence of processing conditions on measured crystallographic texture, pole figures were generated using the same scale to compare maximum intensities between the measured data (α-Ti diffraction patterns) and reconstructed data (prior-β grains) shown in Figure 6. Figure 6 describes three material conditions, two conditions representing the two observed extremes in crystallographic texture and another that exhibits a mixture of texture components. The condition produced with a contour adjusted scan line length of 16 mm produced a texture of $\langle 11\bar{2}0\rangle_\alpha$ parallel to the build direction, whereas the longest contour adjusted scan line length produced a texture of $[0001]_\alpha$ parallel to the build direction. These in turn imply $\langle 100\rangle_\beta$ parallel to the build direction for the shortest case, and $\langle 110\rangle_\beta$ for the longest case during solidification. Textures for all five material conditions were quantified in terms of the percentage of the area in the IPF map of an XY plane that had specified poles lying within 15° of *Z*. Results are tabulated in Table 6. While results vary between material sets produced with differing EBPBF machines and software versions, greater than 80% of the prior-β phase present in the material with scan line length 16 mm had $\langle 100\rangle_\beta$ poles aligned with the build direction. Scan line lengths greater than 46 mm produced prior-β phase (considering bulk/hatch only) with $\langle 110\rangle_\beta$ directions aligned with the build direction (57% to 84%). An intermediate scan line length of 23 mm fell between the two extremes: 14% prior-β phase exhibited $\langle 100\rangle_\beta$ within 15° of *Z*, and 31% had $\langle 110\rangle_\beta$ within 15° of *Z*.

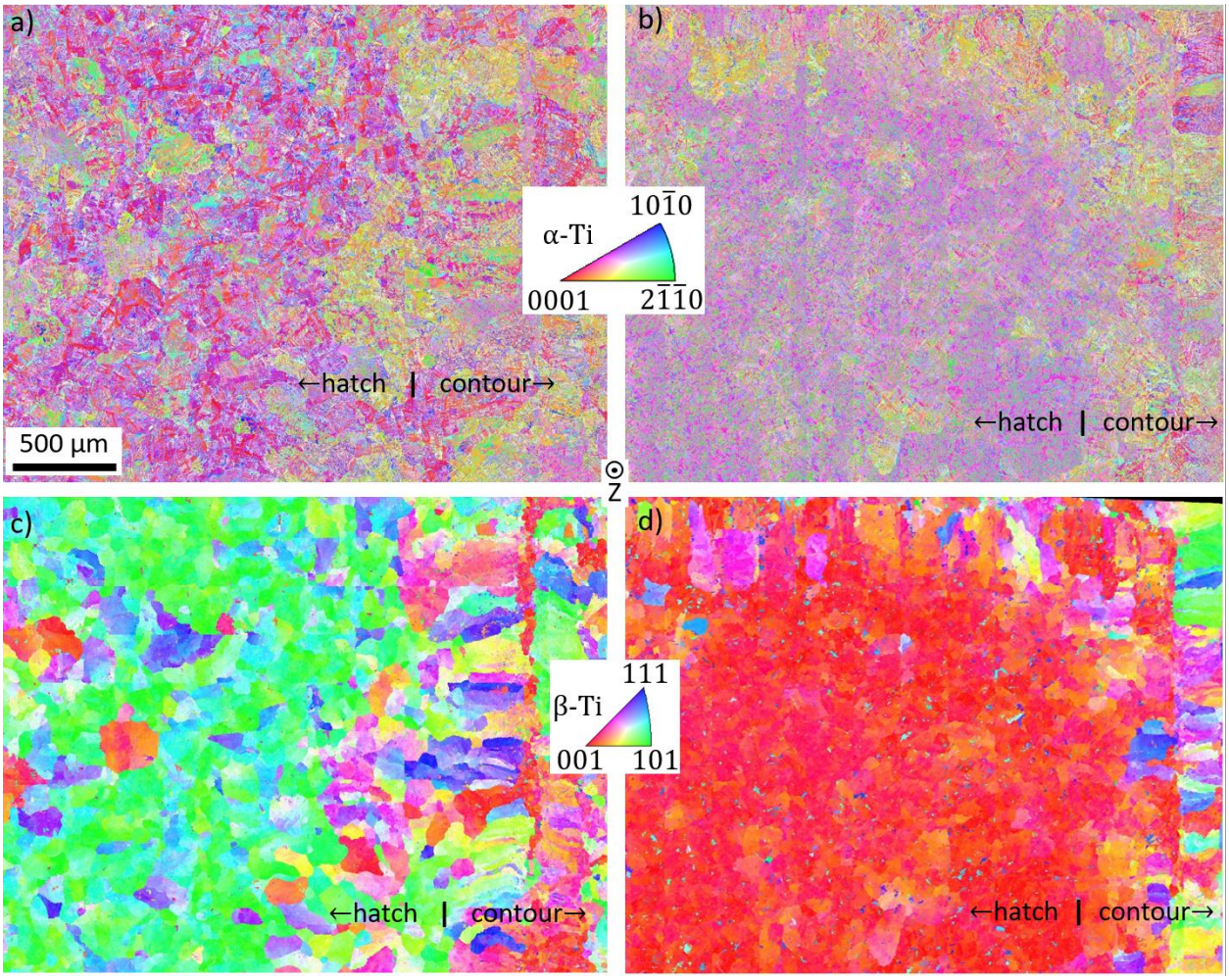

Figure 5: EBSD measurements of α-Ti in the *XY* plane for a) contour adjusted average scan line length of 81 mm and b) 16mm (*Z* is the build direction) for the material set, with the associated prior-β reconstructions c) and d).

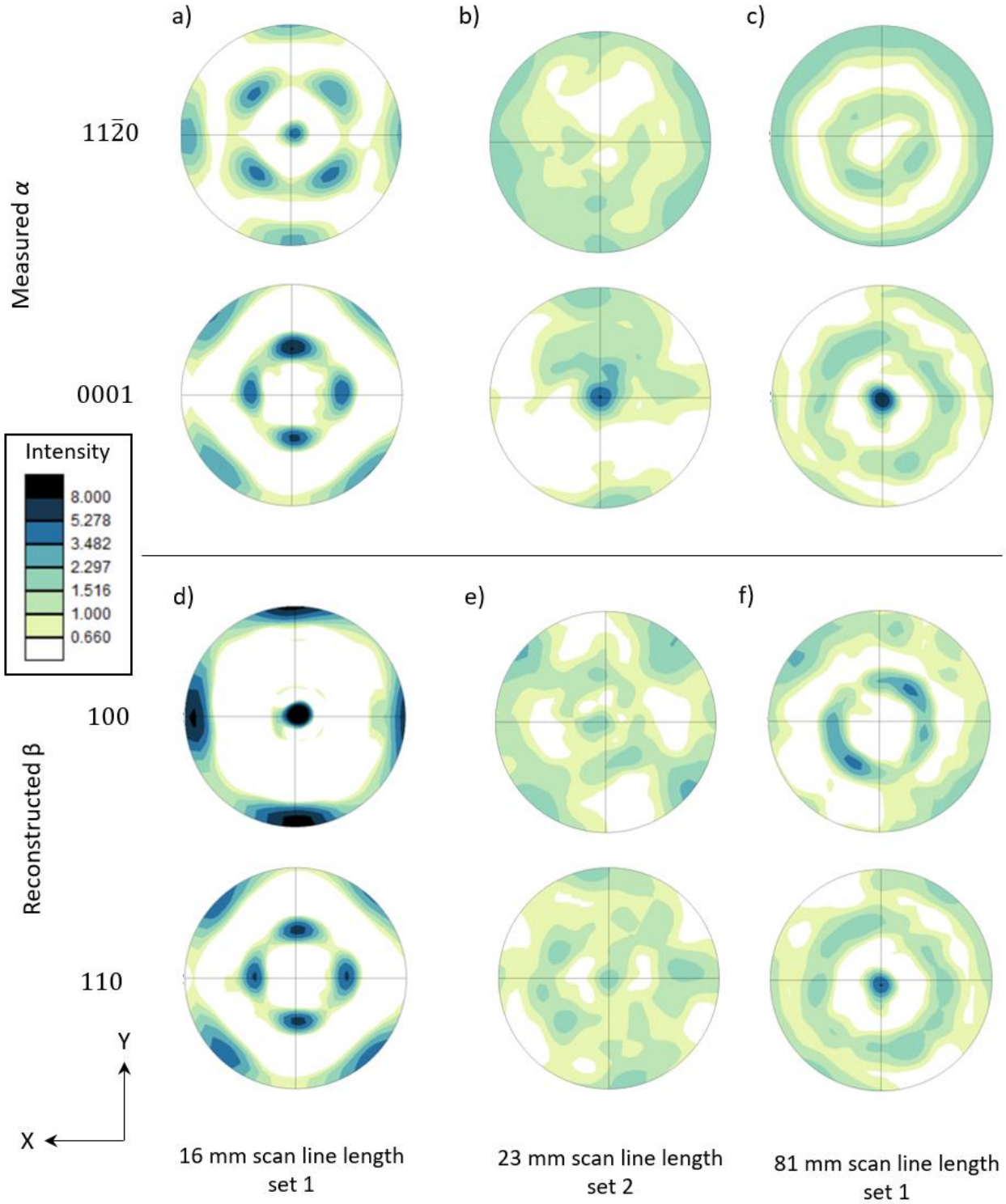

Figure 6: Pole figures for the measure α phase in a to c) and reconstructed prior-β in d to f) for three material conditions that span the full range of measured crystallographic texture parallel to the build direction. The build direction is at the center of the pole figures.

Set	Region	$\overline{l_{p\|\|}}$ [mm]	Area % within 15° of *Z*	
			$\langle 100 \rangle_\beta$	$\langle 110 \rangle_\beta$
1	Bulk	81	3.20	57.5
1	Bulk & Contour	81	7.20	43.4
2	Bulk	69	2.40	82.2
2	Bulk	46	0.68	83.8
2	Bulk	23	14.0	31.0
1	Bulk & Contour	16	71.9	3.58
1	Bulk	16	86.7	0.75

Table 6: Area fractions from the prior-β reconstructions that exhibit selected texture components within 15° of the build direction, *Z*.

3.3 Tensile Properties

Table 7 summarizes quasi-static tensile properties measured for specimen sets 1 and 2 including Young's modulus *E*, 0.2% offset tensile yield strength (s_{YS}), ultimate tensile strength (s_{UTS}), engineering strain at UTS (e_{UTS}), and engineering strain to failure (e_f**)**. The values in Table 7 fall within the broad range of all EBPBF results summarized in Ref. [51], even when filtering those results for test direction and heat treatment status. It is therefore plausible that some of the previously reported variability could be due to unreported line length variations. For comparison, the specification minimum property values from ASTM B348 are also listed, where available. One test from specimen set 1 in the 16 mm scan line length plus HIP condition exhibited the minimum allowable tensile and yield strengths, however all other cases the minimum observed values for each condition exceeded specification minimums from ASTM B348 [34].

Figure 7 shows the engineering stress-strain curves for both specimen sets as well as the true stress strain and strain-hardening behaviors for set 1. In particular, Figure 7a) and b) highlight the plastic region of the engineering stress-strain curves for sets 1 and set 2 respectively. One must keep the oxygen content, surface state, and gage geometry differences in mind when directly comparing sets 1 and 2.

In set 1, there is a consistent increase of 7 to 8% in the yield and ultimate strengths for the long condition vs. the short condition. Additionally, the short condition shows a consistently lower strain at UTS than those observed for the long conditions, though the total strain to failure is similar across both conditions. The overall shape of the stress-strain curves is also notably different, particularly in set 1, with a consistently higher increase in the hardening rate for specimens in the short conditions compared to long. This is quantified in Figure 7 c) and d) in the form of the instantaneous slope of the true stress-strain curve as well as a strain hardening exponent. The specimens exposed to a sub-solvus HIP generally exhibit similar behaviors as their as-built counterparts, though with tensile and ultimate strengths generally decreased by several percent. Even after HIP, the pronounced difference in hardening behavior persists, indicating that while microstructural features governing strength have been modified, persistent differences remain between the sets. Set 2 also shows a consistent increase in tensile and ultimate strengths and strain

at UTS with increasing scan line length. The range of these quantities is not as broad as observed in set 1, but the scan line length range was also smaller.

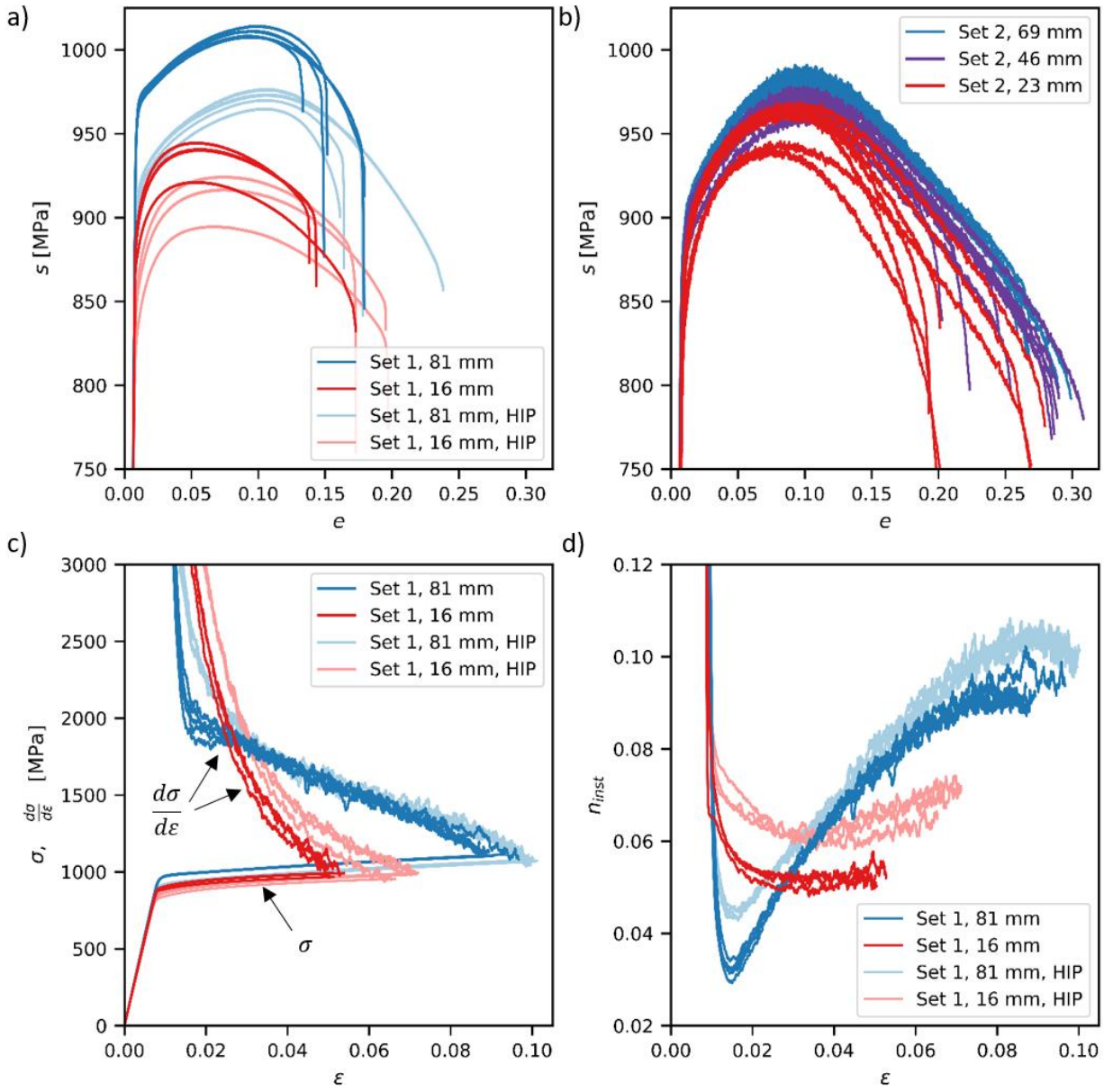

Figure 7: Engineering stress s and strain e for (a) set 1 and (b) set 2 for the range of scan line lengths and post-build heat treatments. (c) Smoothed true stress vs. true strain for set 1, and its instantaneous slope. (d) Instantaneous strain hardening exponent for set 1.

Set	$\overline{l_{p\|\|}}$ [mm]	Heat Treat	Number of specimens	E [GPa]	s_{YS} [MPa]	s_{UTS} [MPa]	e_{UTS} [%]	e_f [%]
1	16	As-built	3	114(1.2)	889(7.9)	936(10.3)	5.4(0.1)	15.2(1.5)
1	16	HIP	3	113(0.4)	847(12.8)	912(12.6)	7.3(0.3)	18.8(1.1)
1	81	As-built	5	117(0.9)	963(2.2)	1011(2.3)	9.5(0.4)	15.8(1.5)
1	81	HIP	4	118(0.4)	907(4.0)	971(4.4)	10.5(0.1)	18.5(3.1)
2	23	As-built	10	107(7.2)	856(14.8)	959(11.0)	8.8(0.6)	23(4.0)
2	46	As-built	10	109(4.5)	880(7.3)	972(5.3)	9.8(0.6)	26.5(3.5)
2	69	As-built	10	109(7.5)	886(4.2)	985(3.57)	9.7(0.4)	27.3(1.8)
Spec. Min.	-	Grade 5	-	-	828	895	-	10
Spec. Min.	-	Grade 23	-	-	759	828	-	10

Table 7: Mechanical property measurements for specimen sets 1 and 2. Values in parentheses indicate one standard deviation about the mean value reported in the respective cell. Note that two of the surfaces on items in specimen set 1 are as-built, and all surfaces for specimen set 2 are fully machined. Specification minimums are from ASTM B348 [34].

3.4 Processing Conditions

In general, Figure 3 shows that each layer exhibits two plateaus in beam current. The order, amplitude, and duration of these plateaus change in a predictable way throughout the periodic scan strategy rotation sequence, allowing a conclusive mapping of the high current plateau with the longer scan line length items, and a lower value for the shorter items. Figure 8 shows the median value of the beam current as a function of the contour adjusted scan line length, as determined from the log-file analysis of data from Figure 3 and using Equation 6. Additionally, Figure 9 shows how the average scanning velocity determined from Equation 6 varies with beam current, and Table 8 summarizes the resulting data needed for model input.

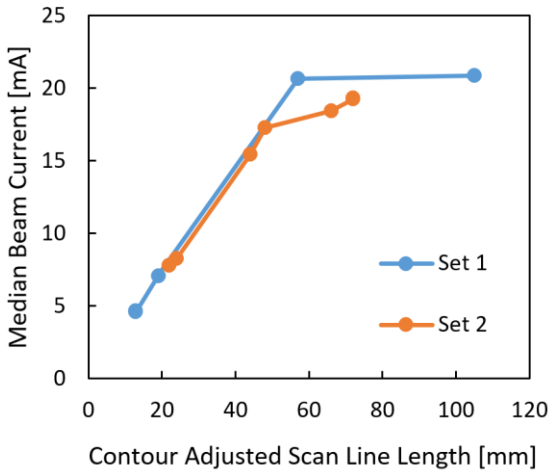

Figure 8: Median beam current as a function of contour adjusted scan line length for both specimen sets, as determined from log-file analysis.

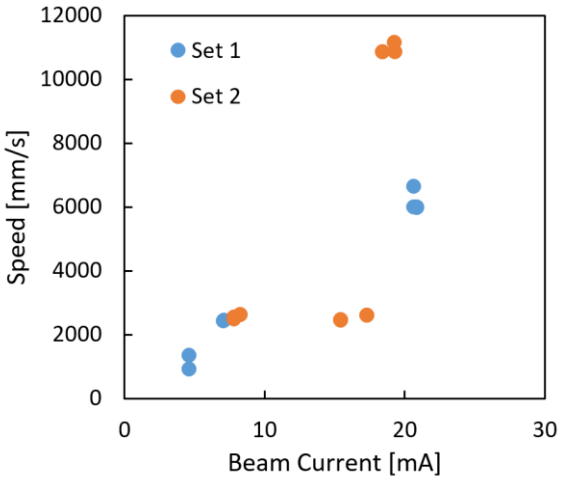

Figure 9: Scanning speed as a function of beam current for both specimen sets, as determined from log-file analysis.

3.5 Process Modeling

The later columns of Table 8 show the modeled dimensions of the melt-pool as it passes through the center of the long and short regions for all scan directions in set 1. While this model uses only rough estimates for the calibration parameters for efficiency and source shape, the overall widths and depths are reasonable given the hatch spacing and layer thickness utilized in the builds, and it is the relative differences that are of primary interest. The short case generally exhibits a wider range of pool sizes across the scan orientations due to the larger relative change in scan line length, and therefore parameters, as discussed in Sec. 3.4. The long case is processed with the same power and speed across the scan orientation sequence, though there is a slight difference in the actual scan length, and therefore the elapsed time between passes. The largest difference between the pool shapes is the ratio of pool length to width, with pools being of significantly higher aspect ratio across all scan orientations for the long case compared to the short. Also, note that while calculations have been performed for all four scan angles, generally the results for angles differing by 180° are essentially the same and are not duplicated in the table.

Condition	$\overline{l_{p\|\|}}$ [mm]	$l_{p\|\|}$ [mm]	Scan Angle [deg]	P_p [W]	v_p [mm/s]	Modeled Melt Pool [µm]			Length/ Width
						Width	Depth	Length	
Long	81	105	0, 180	1250	6000	200.7	100.4	4246.1	21.2
		57	90, 270	1250	6000	212.0	105.9	4823.8	22.8
Short	16	19	0, 180	425	2430	193.7	96.8	1554.8	8.0
		13	90, 270	278	926	252.1	126.1	1130.0	4.5

Table 8: Model parameters that vary with scan line length and resulting melt pool dimensions predicted by the DSM

4 Discussion

While there are a number of differences between sets 1 and 2, an important trend exhibited within each set is an increase in yield and ultimate strength measured along the build direction with increasing scan line length, despite no explicit change in nominal processing conditions within a set. In set 1, increases in both yield and ultimate strengths on the order of 7 to 8% and strain at UTS were observed for the longest scan line length cases compared to the shortest. Set 2 spanned a narrower range of line lengths and also strengths, though the trend in terms of increasing strength

with increasing line length was similar to set 1. There are absolute differences in the strengths exhibited by set 1 compared to set 2, but we also note that there are key differences in the processing parameters (Table 2), and importantly in the oxygen content (Table 3) of both feedstock and as-built material. The generally higher strengths in set 1 are consistent with their increased oxygen content [52], but the critical point is that the trend of increasing strength with increasing line length within each set persists despite the differences in processing and material chemistry between the sets, indicating a pervasive effect of line length on strength.

Analysis of salient microstructural features including prior β grain size and α lath thickness yielded no statistically significant differences as a function of scan line length within either set. There are some differences in porosity content, specifically Set 1 showed a higher pore content in the long line length condition. However, in all cases the overall pore content is small enough that it is not expected to impact quasi-static tensile yield or ultimate strength, though this could be important for fatigue behavior. Two distinct α textures were observed at the extremes of scan line length, implying different prior β textures. Specifically: (i) for shorter scan line lengths $\langle 11\bar{2}0\rangle_\alpha$ were observed to align with the build direction (*Z*), implying prior $\langle 100\rangle_\beta$ alignment with *Z* (Figure 6 a) and d), and similar to Refs. [4], [5], [24]), whereas (ii) for longer scan line lengths $[0001]_\alpha$ was aligned with *Z* implying prior $\langle 110\rangle_\beta$ parallel to the build direction (Figure 6c) and f), similar to lot 1 specimens in reference [7]). As mentioned previously, the case of $\langle 100\rangle_\beta$ grain alignment along the build direction is consistent with many other large-scale texture analysis of EBPBF strategies. While instances of $\langle 110\rangle_\beta$ directions aligned with the build direction have been observed previously, these are less common.

Previous work on single colonies in other α/β titanium alloys has shown that significant strength anisotropies exist [53]–[55]. In terms of macroscopic behavior, Bache and Evans [23] reported preferential $[0001]_\alpha$ alignment along the transverse direction with an intensity 19 times random in rolled Ti-6Al-4V plates. This texture is similar to the long line length conditions in the present study, and they found that tensile behavior along this direction was approximately 9 to 10% higher and strain at UTS roughly 40% higher than that of the longitudinal direction. While the processing mechanism generating the texture differences is different, the present results are consistent with this prior work in both the direction and magnitude of the trends, reinforcing the conclusion that texture is indeed the primary microstructural feature driving the observed mechanical property differences.

While dynamic properties were not evaluated in the present study, work on conventionally fabricated (i.e., wrought) material suggests that quasi-static property differences could translate to much larger changes in fatigue performance. The work of Bache and Evans [23] did evaluate strain-controlled fatigue behavior and observed debits in life in both the low- and high-cycle fatigue regimes of more than 3× for the transverse orientation (along which $[0001]_\alpha$ was preferentially aligned) compared to life for the longitudinal orientation at the same strain rage. The study of Sinha, Mills, and Williams on a similar alloy [56] suggests that 4% increase in yield strength can potentially more than double fatigue and dwell fatigue lives at a given stress for load-controlled tests, and can potentially result in more than 8× increase in creep life at a fixed applied stress. Together, these results indicate that EBPBF Ti-6Al-4V processed with the long and short scan line length conditions would be expected to exhibit significantly different fatigue, dwell-fatigue, and creep properties. Further, the relative fatigue and dwell-fatigue lives for the materials

processed under the two conditions will be expected to depend on whether the tests are conducted in stress-control or strain-control, akin to the prior studies on wrought titanium alloys [23, 56]. Specifically, longer fatigue, dwell-fatigue, and creep lives will be expected under stress-control for materials processed with long scan line lengths than for materials processed with short scan line lengths. In contrast, shorter fatigue and dwell-fatigue lives will be expected under strain-control for materials processed with long line lengths than for materials processed with short line lengths. In view of the variations in texture and quasi-static mechanical properties presented for additively manufactured Ti-6Al-4V in the current study, and the data in literature on the variations of fatigue, dwell-fatigue, and creep properties with quasi-static properties of wrought titanium alloys, an evaluation of fatigue and creep properties of titanium alloys additively manufactured with different scan line lengths merits further investigations. Initial assessments of J-type fracture toughness indicates that scan line length does indeed affect this property by upwards of 40% differences in the critical toughness for crack initiation, and further work is underway [57].

While no explicit processing changes were commanded as a function of the scan line length variation in either set 1 or set 2, the printing system implicitly changes conditions as a function of component geometry. To better understand the impact of these changes, system generated logs of the processing conditions were analyzed to infer location specific processing conditions. These values were in-turn utilized as inputs to a process model to predict details of the solidification process which is responsible for the primary β texture generation. While there are many uncertainties in both the log analysis and the subsequent process modeling exercise, the results generally indicate the likelihood of significant changes in the resulting melt-pool geometry between the long and short cases. The width and depth remain similar across regions with different scan line lengths as quantified in Table 8, and is consistent with the fact that no large changes in the prior-β grain diameter or lack of fusion porosity were observed. However, the length to width aspect ratio is predicted to be significantly different, with a more elongated pool for the long scan line length conditions. While it is common to assess melt pool geometry as a function of the linear energy density P/v, analysis of basic melt-pool scaling indicates that pool length to width aspect ratio is proportional to the square root of the product Pv. Figure 10 shows the area fractions of the orientations in bulk regions quantified in Table 6 as a function of this product for both specimen sets and all $\overline{l_{p||}}$. Bulk regions with conditions $Pv \lesssim 10^6$ W mm s^{-1} are dominated by $\langle 100 \rangle_\beta$, whereas above this value there is a rapid transition to $\langle 110 \rangle_\beta$ or mixed $\langle 110 \rangle_\beta$ and $\langle 111 \rangle_\beta$. Although it is tempting to assess orientation area fraction as a function of scan line length, this is complicated by differences in speed function between Sets 1 and 2 (Table 1). As speed function increases, the acceleration of beam current and scan velocity for a given change in scan line length increases.

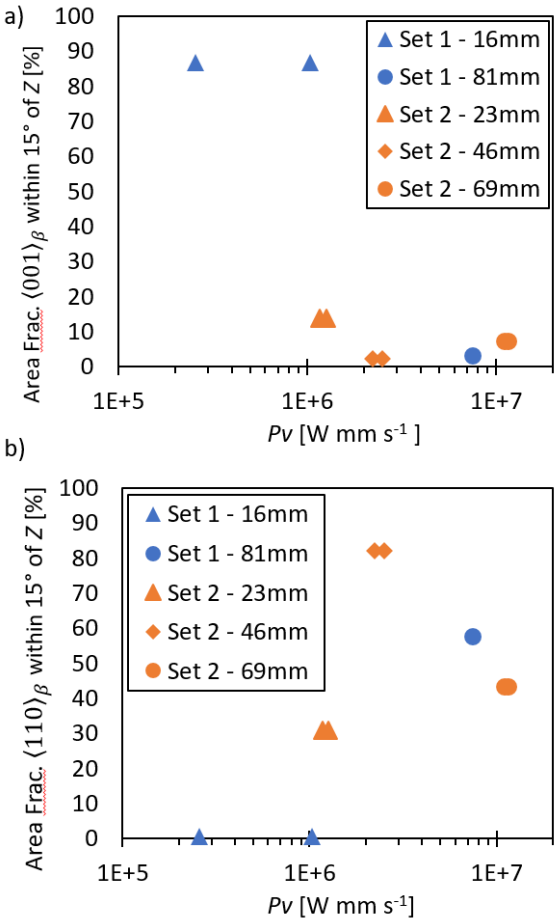

Figure 10: Effect of the product of applied power and scan velocity, Pv on a) area fraction of grains that have $\langle 001 \rangle_\beta$ within 15° of the Z direction, and b) area fraction of grains that have $\langle 110 \rangle_\beta$ within 15° of the Z direction.

The above analysis and modeling exercise are generally instructive of meaningful differences between the scan line length cases, but there are a number of issues that limit its accuracy to a qualitative nature. First, as described in Sec. 2.4, there are a number of approximations and uncertainties in the procedure to extract the key location-specific process parameter values. Greater insight into these values would be highly beneficial and could be achieved either through dedicated process monitoring, direct interaction with the printer's control software, or a combination of these. Additionally, the approach employed was only feasible with simple rectangular geometries and knowledge of how individual bodies were assigned into melt groups, the latter of which may not always be carefully controlled. While this work adds to the existing collection of works that have attempted to assess the relationship between process geometry and conditions, these details are generally subject to enhancements in process planning algorithms and the control software stack used to drive the machines [3], [11]. The generalizability of the presently documented details to other machine models or control software versions must be treated with caution. This issue is not unique to the particular systems used in the present work, but is rather a general challenge in AM and has driven development of a growing selection of open-source powder bed fusion systems.

There are additional compounding challenges beyond those listed above. First, the DSM method employed herein is generally sensitive to local changes in process parameters and scan timing, however it does not directly account for slower time-scale losses due to radiation or conduction of heat through the surrounding bed. Additionally, the present calculation did not explicitly include the input of heat during the contouring or preheating processes. The balance of these effects control the background temperature T_0 which was assumed constant and independent of scan line length. Variation in this quantity across the different regions is certainly possible and could modify the melt-pool geometry differences. Finally, key calibration parameters were only roughly estimated, particularly the efficiency η and the source shape σ_x/σ_z. In laser powder bed fusion these are known to vary significantly as a function of laser power [58], though less is known for the EBPBF process. Given the range of P and v exhibited in Table 8, it is plausible that these could vary significantly, and additional dedicated experiments are needed to identify appropriate values, similar to those in ref. [49].

Finally, while the present analysis focused on melt-pool shape, a full explanation of the actual grain morphology and particularly the texture development must consider the solidification process in more detail. A range of solidification models have been developed in the context of casting, and have been increasingly applied to AM processes [59], [60]. The importance of the interaction of the AM scan strategy details with the physics of both nucleation and the patterning of solidification from grains generated in previous layers and only partially remelted is likely critical. Scan paths that either reinforce or break the underlying crystallographic symmetries could be employed to promote different desired textures, or lack thereof.

Another important point is that the texture effect was resilient despite at least some differences in the processing conditions between set 1 and set 2. In particular, speed functions of 98 and 76 were employed for sets 1 and 2 respectively. Previous work on EBPBF Ti-6Al-4V shows that as speed function increases, melt pool area decreases exponentially, though it changes minimally at speed functions greater than 50 [11]. That work also established a positive linear trend between prior-β grain width and melt pool width. In the present study, the measured prior-β grain width was not significantly different between material conditions as shown in Table 5, and this is also consistent with minimal differences in melt pool width in Table 8.

This study has demonstrated that changes in scan line length lead to significant changes in texture (Figure 10) and tensile properties (up to 8% in UTS and YS). For Set 2, these changes occur between identical part geometries that could be directly adjacent to each other on the same build plate. This has potentially significant negative implications on industrial production environments if scan line length variation is not controlled and minimized. It is also important to note that the scan line length range over which these significant changes in texture and tensile properties are occurring is well below the EBPBF machine manufacturer recommended maximum scan line length (90 mm [9]) to avoid increased amounts of lack of fusion porosity formation.

5 Summary and Conclusions

Global input processing parameters were held constant during EBPBF fabrication of Ti-6Al-4V in each of two different build geometries. Variations in crystallographic texture and tensile properties resulted from the EBPBF system adjusting to geometry changes in the form of scan line length variations of 5×. The conclusions of this study are summarized below:

1. Processing under long and short scan line lengths resulted in similar α lath thickness, prior β grain size, and β volume fraction, however the $[0001]_\alpha$ direction was strongly aligned with the build direction for the long condition, whereas $\langle 11\bar{2}0\rangle_\alpha$ directions were aligned with the build direction for the short case. This texture is consistent with as-solidified prior β texture with $\langle 110\rangle_\beta$ and $\langle 100\rangle_\beta$ aligned with the build direction for long and short conditions, respectively. The rapid transition between these textures has been linked to the product of the processing power and speed, Pv.

2. The tensile yield and ultimate strengths along the build direction were up to 8% higher for the long scan vs. short scan line length. The strain hardening exponent was relatively constant for the short line length condition, but increased with strain for the long line length condition.

3. A sub-transus HIP treatment resulted in a reduction of porosity and coarsening of microstructure for both the long and short scan line lengths, but did not change the textures appreciably. HIP reduced the tensile yield strength of as-built materials by approximately 5-6%, and ultimate tensile strength by 3-4%.

4. Understanding the mechanisms of formation of crystallographic texture as a function of location specific process parameters is important for its control, whether to promote or inhibit certain textures as desired for a particular application, for design of appropriate post-processing operations, and for assessing the applicability and limitations of mechanical property databases within a component design context.

6 Author Contributions:

EJS: conceptualization, software, formal analysis, investigation, writing - original draft, writing – review & editing, visualization, supervision
JTB: conceptualization, formal analysis, investigation, writing - original draft, writing - review & editing, visualization, supervision
VS: writing - original draft, writing - review & editing, visualization, formal analysis, investigation
TMB: methodology, software, validation, formal analysis, investigation, writing original draft and review & editing
KJC: conceptualization, validation, formal analysis, investigation, visualization
ALP: software, formal analysis, writing - review & editing
NDS: formal analysis, investigation, data curation, writing - original draft
RJ: conceptualization, formal analysis, investigation, writing - review & editing, visualization, supervision.
NH: conceptualization, formal analysis, investigation, writing - original draft, writing - review & editing, visualization, supervision

7 Acknowledgments:

The authors thank Jared Shank (UES, Inc.) and Nathan Levkulich (UES, Inc.) for help with EBSD data acquisition, Dr. Dennis J. Buchanan (UDRI) for specimen design, Rob Turner (UES,

Inc.) for assistance with HIP, and Dr. Ryan Dehoff (ORNL) for assistance with specimen fabrication.

Data Availability: The raw/processed data required to reproduce these findings cannot be shared at this time due to technical or time limitations.

8 References

[1] S. Liu and Y. C. Shin, "Additive manufacturing of Ti6Al4V alloy: A review," *Materials & Design*, vol. 164, p. 107552, Feb. 2019, doi: 10.1016/j.matdes.2018.107552.

[2] G. Lütjering and J. C. Williams, *Titanium*, 2nd ed. Berlin Heidelberg: Springer-Verlag, 2007. doi: 10.1007/978-3-540-73036-1.

[3] T. Mahale, "Electron Beam Melting of Advanced Materials and Structures," North Carolina State University, Raleigh, North Carolina, 2009. [Online]. Available: http://www.lib.ncsu.edu/resolver/1840.16/4943

[4] S. S. Al-Bermani, M. L. Blackmore, W. Zhang, and I. Todd, "The Origin of Microstructural Diversity, Texture, and Mechanical Properties in Electron Beam Melted Ti-6Al-4V," *Metall Mater Trans A*, vol. 41, no. 13, pp. 3422–3434, Dec. 2010, doi: 10.1007/s11661-010-0397-x.

[5] A. A. Antonysamy, J. Meyer, and P. B. Prangnell, "Effect of build geometry on the β-grain structure and texture in additive manufacture of Ti6Al4V by selective electron beam melting," *Materials Characterization*, vol. 84, pp. 153–168, Oct. 2013, doi: 10.1016/j.matchar.2013.07.012.

[6] B. Cheng, S. Price, X. Gong, J. Lydon, K. Cooper, and K. Chou, "Speed Function Effects in Electron Beam Additive Manufacturing," presented at the ASME 2014 International Mechanical Engineering Congress and Exposition, Mar. 2015. doi: 10.1115/IMECE2014-36664.

[7] S. L. Draper *et al.*, "Materials Characterization of Electron Beam Melted Ti-6Al-4V," NASA, NASA/TM—2016-219136, Sep. 2016. doi: 10.1002/9781119296126.ch242.

[8] X. Tan *et al.*, "Revealing martensitic transformation and α/β interface evolution in electron beam melting three-dimensional-printed Ti-6Al-4V," *Sci Rep*, vol. 6, no. 1, p. 26039, May 2016, doi: 10.1038/srep26039.

[9] N. Hrabe, T. Gnäupel-Herold, and T. Quinn, "Fatigue properties of a titanium alloy (Ti–6Al–4V) fabricated via electron beam melting (EBM): Effects of internal defects and residual stress," *International Journal of Fatigue*, vol. 94, pp. 202–210, Jan. 2017, doi: 10.1016/j.ijfatigue.2016.04.022.

[10] W. Everhart, J. Dinardo, and C. Barr, "The Effect of Scan Length on the Structure and Mechanical Properties of Electron Beam-Melted Ti-6Al-4V," *Metall Mater Trans A*, vol. 48, no. 2, pp. 697–705, Feb. 2017, doi: 10.1007/s11661-016-3866-z.

[11] S. P. Narra, R. Cunningham, J. Beuth, and A. D. Rollett, "Location specific solidification microstructure control in electron beam melting of Ti-6Al-4V," *Additive Manufacturing*, vol. 19, pp. 160–166, Jan. 2018, doi: 10.1016/j.addma.2017.10.003.

[12] M. Majdic and G. Ziegler, "Effect of the Metastable beta -Phase Transformations in the Ti-6Al-4V Alloy.," *Zeitschrift fuer Metallkunde/Materials Research and Advanced Techniques*, vol. 64, no. 11, pp. 751–758, 1973.

[13] T. Ahmed and H. J. Rack, "Phase transformations during cooling in α+β titanium alloys," *Materials Science and Engineering: A*, vol. 243, no. 1, pp. 206–211, Mar. 1998, doi: 10.1016/S0921-5093(97)00802-2.

[14] W. G. Burgers, "On the process of transition of the cubic-body-centered modification into the hexagonal-close-packed modification of zirconium," *Physica*, vol. 1, no. 7–12, pp. 561–586, May 1934, doi: 10.1016/S0031-8914(34)80244-3.

[15] "Orientation relationships in precipitation systems," *Acta Metallurgica*, vol. 30, no. 1, pp. 63–73, Jan. 1982, doi: 10.1016/0001-6160(82)90045-1.
[16] T. Furuhara, T. Ogawa, and T. Maki, "Atomic structure of interphase boundary of an a precipitate plate in a β Ti[sbnd]Cr alloy," *Philosophical Magazine Letters*, vol. 72, no. 3, pp. 175–183, Sep. 1995, doi: 10.1080/09500839508242449.
[17] P. A. Kobryn and S. L. Semiatin, "Microstructure and texture evolution during solidification processing of Ti–6Al–4V," *Journal of Materials Processing Technology*, vol. 135, no. 2–3, pp. 330–339, Apr. 2003, doi: 10.1016/S0924-0136(02)00865-8.
[18] J. Gockel, J. Beuth, and K. Taminger, "Integrated control of solidification microstructure and melt pool dimensions in electron beam wire feed additive manufacturing of Ti-6Al-4V," *Additive Manufacturing*, vol. 1–4, pp. 119–126, Oct. 2014, doi: 10.1016/j.addma.2014.09.004.
[19] J. Gockel, J. Fox, J. Beuth, and R. Hafley, "Integrated melt pool and microstructure control for Ti–6Al–4V thin wall additive manufacturing," *Materials Science and Technology*, vol. 31, no. 8, pp. 912–916, Jun. 2015, doi: 10.1179/1743284714Y.0000000704.
[20] J. Gockel, L. Sheridan, S. P. Narra, N. W. Klingbeil, and J. Beuth, "Trends in Solidification Grain Size and Morphology for Additive Manufacturing of Ti-6Al-4V," *JOM*, vol. 69, no. 12, pp. 2706–2710, Dec. 2017, doi: 10.1007/s11837-017-2601-6.
[21] V. Hasija, S. Ghosh, M. J. Mills, and D. S. Joseph, "Deformation and creep modeling in polycrystalline Ti–6Al alloys," *Acta Materialia*, vol. 51, no. 15, pp. 4533–4549, Sep. 2003, doi: 10.1016/S1359-6454(03)00289-1.
[22] M. F. Savage, J. Tatalovich, M. Zupan, K. J. Hemker, and M. J. Mills, "Deformation mechanisms and microtensile behavior of single colony Ti–6242Si," *Materials Science and Engineering: A*, vol. 319–321, pp. 398–403, Dec. 2001, doi: 10.1016/S0921-5093(01)01024-3.
[23] M. R. Bache and W. J. Evans, "Impact of texture on mechanical properties in an advanced titanium alloy," *Materials Science and Engineering: A*, vol. 319–321, pp. 409–414, Dec. 2001, doi: 10.1016/S0921-5093(00)02034-7.
[24] C. de Formanoir, S. Michotte, O. Rigo, L. Germain, and S. Godet, "Electron beam melted Ti–6Al–4V: Microstructure, texture and mechanical behavior of the as-built and heat-treated material," *Materials Science and Engineering: A*, vol. 652, pp. 105–119, Jan. 2016, doi: 10.1016/j.msea.2015.11.052.
[25] N. Hrabe, R. White, and E. Lucon, "Effects of internal porosity and crystallographic texture on Charpy absorbed energy of electron beam melting titanium alloy (Ti-6Al-4V)," *Materials Science and Engineering: A*, vol. 742, pp. 269–277, Jan. 2019, doi: 10.1016/j.msea.2018.11.005.
[26] P. Fernandez-Zelaia *et al.*, "Crystallographic texture evolution in electron beam melting additive manufacturing of pure Molybdenum," *Materials & Design*, vol. 207, p. 109809, Sep. 2021, doi: 10.1016/j.matdes.2021.109809.
[27] Z. R. Francis, "The Effects of Laser and Electron Beam Spot Size in Additive Manufacturing Processes," Carnegie Mellon University, Pittsburgh, PA, 2017. [Online]. Available: 10.1184/R1/6723563.v1
[28] T. Nagase, T. Hori, M. Todai, S.-H. Sun, and T. Nakano, "Additive manufacturing of dense components in beta-titanium alloys with crystallographic texture from a mixture of pure metallic element powders," *Materials & Design*, vol. 173, p. 107771, Jul. 2019, doi: 10.1016/j.matdes.2019.107771.

[29] Q. Zhang, J. Chen, P. Guo, H. Tan, X. Lin, and W. Huang, "Texture and microstructure characterization in laser additive manufactured Ti–6Al–2Zr–2Sn–3Mo–1.5Cr–2Nb titanium alloy," *Materials & Design*, vol. 88, pp. 550–557, Dec. 2015, doi: 10.1016/j.matdes.2015.09.053.
[30] M. Simonelli, Y. Y. Tse, and C. Tuck, "Effect of the build orientation on the mechanical properties and fracture modes of SLM Ti–6Al–4V," *Materials Science and Engineering: A*, vol. 616, pp. 1–11, Oct. 2014, doi: 10.1016/j.msea.2014.07.086.
[31] M. Simonelli, Y. Y. Tse, and C. Tuck, "On the Texture Formation of Selective Laser Melted Ti-6Al-4V," *Metall Mater Trans A*, vol. 45, no. 6, pp. 2863–2872, Jun. 2014, doi: 10.1007/s11661-014-2218-0.
[32] D. Kumar, G. Shankar, K. G. Prashanth, and S. Suwas, "Texture dependent strain hardening in additively manufactured stainless steel 316L," *Materials Science and Engineering: A*, vol. 820, p. 141483, Jul. 2021, doi: 10.1016/j.msea.2021.141483.
[33] 14:00-17:00, "ISO/ASTM 52921:2013." Accessed: May 26, 2021. [Online]. Available: https://www.iso.org/cms/render/live/en/sites/isoorg/contents/data/standard/06/27/62794.html
[34] ASTM International, "ASTM B348 - Standard Specification for Titanium and Titanium Alloy Bars and Billets," 2019.
[35] SAE International, "AMS4992C: Casting, Structural Investment, Titanium Alloy 6Al - 4V Hot Isostatically Pressed," 2018.
[36] J. Schindelin *et al.*, "Fiji: an open-source platform for biological-image analysis," *Nature Methods*, vol. 9, no. 7, pp. 676–682, Jul. 2012, doi: 10.1038/nmeth.2019.
[37] P. C. Collins, B. Welk, T. Searles, J. Tiley, J. C. Russ, and H. L. Fraser, "Development of methods for the quantification of microstructural features in α+β-processed α/β titanium alloys," *Materials Science and Engineering: A*, vol. 508, no. 1–2, pp. 174–182, May 2009, doi: 10.1016/j.msea.2008.12.038.
[38] J. Tiley *et al.*, "Quantification of microstructural features in α/β titanium alloys," *Materials Science and Engineering: A*, vol. 372, no. 1–2, pp. 191–198, May 2004, doi: 10.1016/j.msea.2003.12.008.
[39] T. Searles *et al.*, "Rapid characterization of titanium microstructural features for specific modelling of mechanical properties," *Meas. Sci. Technol.*, vol. 16, no. 1, pp. 60–69, Dec. 2004, doi: 10.1088/0957-0233/16/1/009.
[40] H. J. G. Gundersen, T. B. Jensen, and R. Østerby, "Distribution of Membrane Thickness Determined By Lineal Analysis," *Journal of Microscopy*, vol. 113, no. 1, pp. 27–43, 1978, doi: https://doi.org/10.1111/j.1365-2818.1978.tb00091.x.
[41] A. R. Shiveley, P. A. Shade, A. L. Pilchak, J. S. Tiley, and R. Kerns, "A novel method for acquiring large-scale automated scanning electron microscope data," *Journal of Microscopy*, vol. 244, no. 2, pp. 181–186, Nov. 2011, doi: 10.1111/j.1365-2818.2011.03524.x.
[42] A. L. Pilchak, A. R. Shiveley, J. S. Tiley, and D. L. Ballard, "AnyStitch: a tool for combining electron backscatter diffraction data sets: ANYSTITCH," *Journal of Microscopy*, vol. 244, no. 1, pp. 38–44, Oct. 2011, doi: 10.1111/j.1365-2818.2011.03496.x.
[43] A. I. Saville *et al.*, "Texture evolution as a function of scan strategy and build height in electron beam melted Ti-6Al-4V," *Additive Manufacturing*, vol. 46, p. 102118, Oct. 2021, doi: 10.1016/j.addma.2021.102118.

[44] A. L. Pilchak and J. C. Williams, “Microstructure and Texture Evolution during Friction Stir Processing of Fully Lamellar Ti-6Al-4V,” *Metall and Mat Trans A*, vol. 42, no. 3, pp. 773–794, Mar. 2011, doi: 10.1007/s11661-010-0434-9.
[45] M. G. Glavicic, P. A. Kobryn, T. R. Bieler, and S. L. Semiatin, “A method to determine the orientation of the high-temperature beta phase from measured EBSD data for the low-temperature alpha phase in Ti-6Al-4V,” *Materials Science and Engineering: A*, vol. 346, no. 1–2, pp. 50–59, Apr. 2003, doi: 10.1016/S0921-5093(02)00535-X.
[46] M. G. Glavicic, P. A. Kobryn, T. R. Bieler, and S. L. Semiatin, “An automated method to determine the orientation of the high-temperature beta phase from measured EBSD data for the low-temperature alpha-phase in Ti–6Al–4V,” *Materials Science and Engineering: A*, vol. 351, no. 1, pp. 258–264, Jun. 2003, doi: 10.1016/S0921-5093(02)00844-4.
[47] C. Cayron, “Groupoid of orientational variants,” *Acta Crystallogr A Found Crystallogr*, vol. 62, no. 1, pp. 21–40, Jan. 2006, doi: 10.1107/S010876730503686X.
[48] A. L. Pilchak, “The effect of friction stir processing on the microstructure, mechanical properties and fracture behavior of investment cast Ti-6Al-4V,” The Ohio State University, 2009. Accessed: May 26, 2021. [Online]. Available: https://etd.ohiolink.edu/apexprod/rws_olink/r/1501/10?clear=10&p10_accession_num=osu1243874522
[49] E. J. Schwalbach, S. P. Donegan, M. G. Chapman, K. J. Chaput, and M. A. Groeber, “A discrete source model of powder bed fusion additive manufacturing thermal history,” *Additive Manufacturing*, vol. 25, pp. 485–498, Jan. 2019, doi: 10.1016/j.addma.2018.12.004.
[50] K. C. Mills, *Recommended Values of Thermophysical Properties for Selected Commercial Alloys*, 1st ed. Woodhead Publishing Ltd and ASM International, 2002. Accessed: May 26, 2021. [Online]. Available: https://www.elsevier.com/books/recommended-values-of-thermophysical-properties-for-selected-commercial-alloys/mills/978-1-85573-569-9
[51] J. J. Lewandowski and M. Seifi, “Metal Additive Manufacturing: A Review of Mechanical Properties,” *Annual Review of Materials Research*, vol. 46, no. 1, pp. 151–186, 2016, doi: 10.1146/annurev-matsci-070115-032024.
[52] R. Boyer, G. Welsch, and E. W. Collings, *Materials Properties Handbook - Titanium Alloys*. Materials Park, OH: ASM International, 1994.
[53] S. Suri, G. B. Viswanathan, and T. Neeraj, “Room temperature deformation and mechanisms of slip transmission in oriented single-colony crystals of and α/β titanium alloy,” *Acta Materialia*, vol. 47, no. 3, pp. 1019–1034, 1999, doi: 10.1016/S1359-6454(98)00364-4.
[54] M. F. Savage, J. Tatalovich, and M. J. Mills, “Anisotropy in the room-temperature deformation of α – β colonies in titanium alloys: role of the α – β interface,” *Philosophical Magazine*, vol. 84, no. 11, pp. 1127–1154, Apr. 2004, doi: 10.1080/14786430320001583O5.
[55] F. Bridier, P. Villechaise, and J. Mendez, “Analysis of the different slip systems activated by tension in a α/β titanium alloy in relation with local crystallographic orientation,” *Acta Materialia*, vol. 53, no. 3, pp. 555–567, Feb. 2005, doi: 10.1016/j.actamat.2004.09.040.
[56] V. Sinha, M. J. Mills, and J. C. Williams, “Understanding the Contributions of Normal-Fatigue and Static Loading to the Dwell Fatigue in a Near-Alpha Titanium Alloy,” *METALLURGICAL AND MATERIALS TRANSACTIONS A*, p. 8.
[57] E. Lucon, J. Benzing, and N. Hrabe, “Room temperature fracture toughness characterization of additively manufactured Ti-6Al-4V,” National Institute of Standards and Technology, Gaithersburg, MD, NIST TN 2065, Sep. 2019. doi: 10.6028/NIST.TN.2065.

[58] J. Trapp, A. M. Rubenchik, G. Guss, and M. J. Matthews, “In situ absorptivity measurements of metallic powders during laser powder-bed fusion additive manufacturing,” *Applied Materials Today*, vol. 9, pp. 341–349, Dec. 2017, doi: 10.1016/j.apmt.2017.08.006.
[59] H. L. Wei, J. Mazumder, and T. DebRoy, “Evolution of solidification texture during additive manufacturing,” *Sci Rep*, vol. 5, no. 1, p. 16446, Nov. 2015, doi: 10.1038/srep16446.
[60] T. M. Rodgers, J. D. Madison, and V. Tikare, “Simulation of metal additive manufacturing microstructures using kinetic Monte Carlo,” *Computational Materials Science*, vol. 135, pp. 78–89, Jul. 2017, doi: 10.1016/j.commatsci.2017.03.053.